Tunable Microcavities Coupled to Rare-Earth Quantum Emitters: Supplement1

KANGWEI XIA [1,6,*], FIAMMETTA SARDI [1,6,*], COLIN SAUERZAPF [1], THOMAS KORNHER [2], HANS-WERNER BECKER[3], ZSOLT KIS 4, LASZLO KOVACS [4], ROMAN KOLESOV [1], JÖRG WRACHTRUP [1,5]

1. 3. Physikalisches Institut, University of Stuttgart, 70569 Stuttgart, Germany.
2. Lumiphase AG, 8802 Kilchberg, Switzerland
3. RUBION, Ruhr-Universität Bochum, 44780 Bochum, Germany.
4. Wigner Research Center for Physics, Institute for Solid State Physics and Optics, H-1121 Budapest, Hungary.
5. Max Planck Institute for Solid State Research, 70569 Stuttgart, Germany
6. These authors contributed equally: Kangwei Xia, Fiammetta Sardi
**Correspondence and requests for materials should be addressed to kangwei.xia@pi3.uni-stuttgart.de, f.sardi@pi3.uni-stuttgart.de*

1. Experimental Setup

(1) Experimental setup for hole-burning spectroscopy

Hole-burning spectroscopy is a method that bleaches the absorption spectrum of a material in the frequency domain. It results in a decrease emission (a "spectral hole") at the selected frequency range. This technique is frequently involved in the investigation of properties of single ions embedded in ensembles. To demonstrate hole-burning spectroscopy, pump and probe lasers with certain frequency detuning are required. Experimentally, the generation of a pump and a probe laser beam for the spectral hole burning was achieved by splitting one laser beam passing through two acousto-optic modulators (AOM)s in double pass configuration as illustrated in Fig. S1. The second AOM was necessary to put the pump laser into the spectral sweeping range of the probe laser. The frequency detuning of -150 MHz to +150 MHz between the pump and probe laser was achieved.

To focus the pump and probe laser beam into the Yb:LN-bulk or Yb:LN-waveguide sample and measure the fluorescence, confocal microscopy working at cryogenic temperature was used. Here, the incoming laser beam was reflected in a 10/90 beamsplitter and then focused with an objective lens into a set depth of the sample. The sample was mounted to a movable stage, to be able to focus the light into the Yb:LN-waveguide at any position and depth. The stage was mounted inside a cryostat, which allows for performing experiments on the sample in different cryogenic temperatures. The emitted light from the sample, as well as the reflected laser light was passing through the same beamsplitter. A $\lambda = 1\mu m$ longpass filter blocked scattered laser light, as well as

some emitted light from impurities found in the LN crystal. Finally, the emitted photons were detected by a superconducting single photon detector (SNSPD).

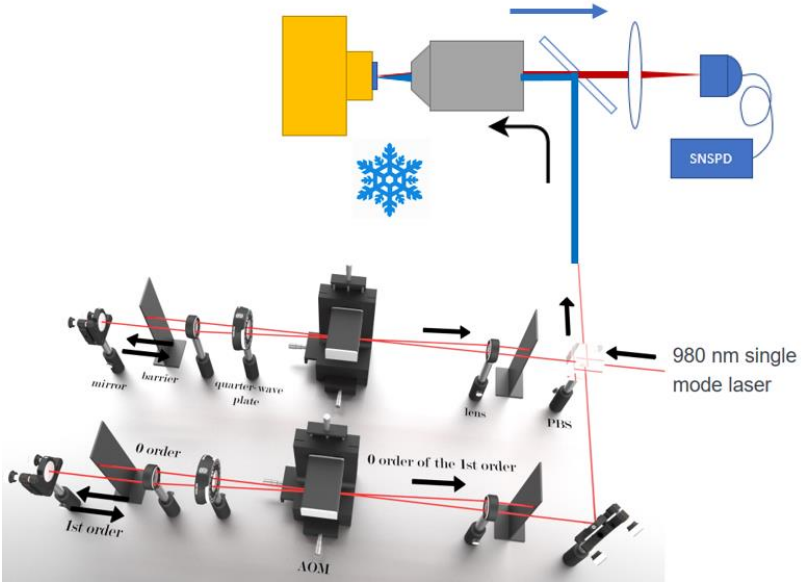

Fig. S1. *Experimental setup for hole burning spectroscopy. AOM: acousto-optic modulator, SNSPD: superconducting single photon detector.*

(2) Experimental setup for cavity pre-characterization

After the shaping of the microcavities on LN thin film, the pre-characterization of the microcavities has been performed at room temperature. The experimental setup is shown in Fig. S2. A home-built single mode diode laser wavelength at 980 nm was applied as the excitation laser. The laser was typically focused at the end of the waveguide to inject the light inside. The emission fluorescence was collected with the same objective lens. The collected fluorescence was sent through a 4f telescope and a galvo mirror and eventually coupled to the SNSPD. A λ = 1μm longpass filter blocked scattered laser light, as well as some emitted light from impurities found in the LN crystal. The scanning of the galvo system suggests how the Yb fluorescence inside the cavity. When the laser was on resonance with the cavity, the cavity lighted up as shown inset graph in Fig. S2. By sweeping the laser frequency, we are able to determine the Q-factor and the resonance frequency of the cavities at room temperature. After pre-characterization of the cavities, the electrodes will be placed on the top of the cavity, which will be introduced in Note 3.

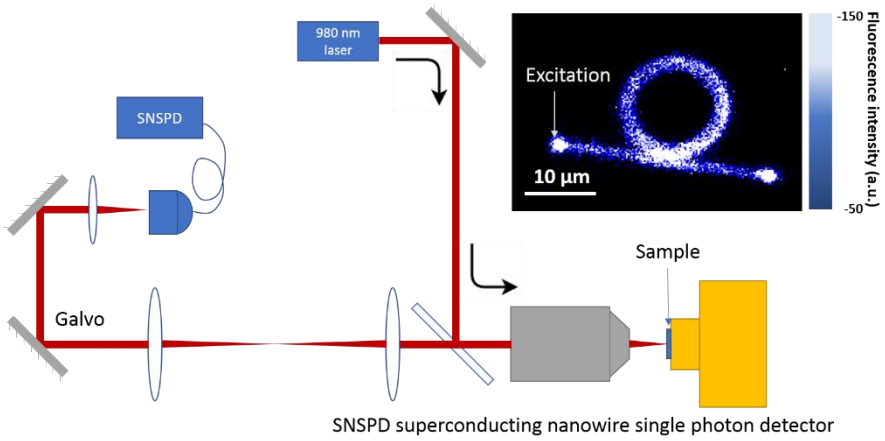

Fig. S2. *Experimental setup for sample pre-characterization. Insert figure: The fluorescence image when the cavity was on resonance with the laser. The emission of* $\boldsymbol{Yb^{3+}}$ *ions has been collected.*

(3) Experimental setup for cavities

For the cavity QED experiments, the pre-characterized microcavities were mounted on the cold finger. The experimental protocol was similar to Fig. S2, however, instead of detecting the downconversion fluorescence of Yb:LN, we need to perform the resonant excitation and resonant detection to determine the Purcell enhancement of the Yb ions in the microcavities. To achieve the highest detection efficiency, we used the mechanical chopper to block the excitation laser and let the fluorescence pass. The measurement protocol is shown in Fig. S3. The mechanical chopper switched the diode laser with a frequency of 10 kHz and 50% duty cycle. The signal of the photodiode was sent to the AOMs to control the excitation laser switching on and off. Two single-path AOMs results in the extinction of the laser light measured to be 53 dB. When the laser was turned on, the Yb:LN was excited. The chopper blocked the laser signal in front of the SNSPD. When the laser was blocked, the Yb still decayed back to the ground state with emitting fluorescence photons. At the same time, the chopper opened in front of the SNSPD. Thus, the SNSPD received the fluorescence photons only coming from the Yb3+:LN. In the experiment, a 1 µm shortpass filter was placed to make sure only the photons from the zero phonon line of Yb:LN arrived at the SNSPD.

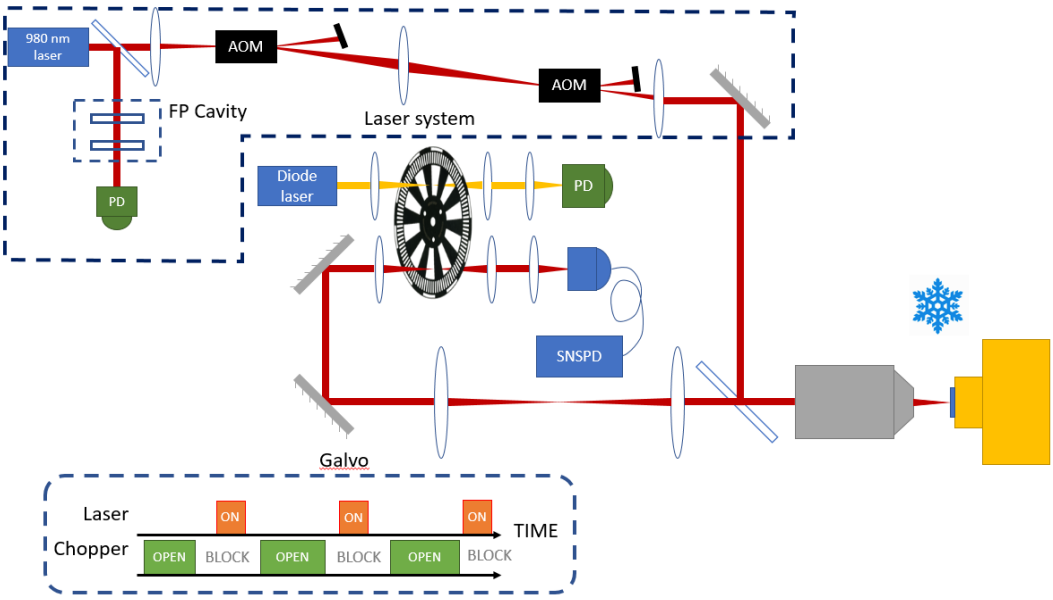

Fig. S3. *Experimental setup for cavity experiments with the pulse scheme. The chopper opened when the laser was turned off to ensure only the fluorescence signal from* $\boldsymbol{Yb^{3+}}$ *was detected.*

2. Yb^{3+} ion implantation

The undoped z-cut LN thin film wafer was bought from NANOLN. The thickness of the LN was measured to be 470 nm. Yb+ ions were implanted successively on the full surface of the LN thin film. The energy and dose of ion implantation had to be properly tuned to have the highest amount of ions in the center of the structures, namely in the center of future waveguides.

According to the stopping and range of ions in matter (SRIM) simulation, inserting the density of LN in the parameters for the implantation, with an energy of 1.5 MeV the depth of the Gaussian profile implantation was centered at 261(71) nm (Fig S4.b), which corresponded to the middle of the LN thin film. Different fluencies were selected in order to have enough signal from the ions but at the same time to avoid cross-talking between electric dipoles and possible cracking caused by implantation.

The implantation doses were between 10^{11}ions/cm^2 and 3×10^{12} ions/cm^2. In the rest of the experiments 10^{12}ions/cm^2 was used.

After implantation, LN thin films were annealed to recover from implantation damages and to activate REIs. For the thermic coefficient mismatch the temperature could not go over 750 °C or the film cracked as shown in Fig S4.c. In order to prevent cracking of the chips, a ramp in the temperature was applied to reach the highest temperature possible. The annealing was divided into

five heating and cooling cycles. The slope at which sample was heated/cooled was 5 °C/min, with an 8 h at the reached temperature. The spectroscopy study of implanted Yb LN thin film will be introduced in SM Note 4.

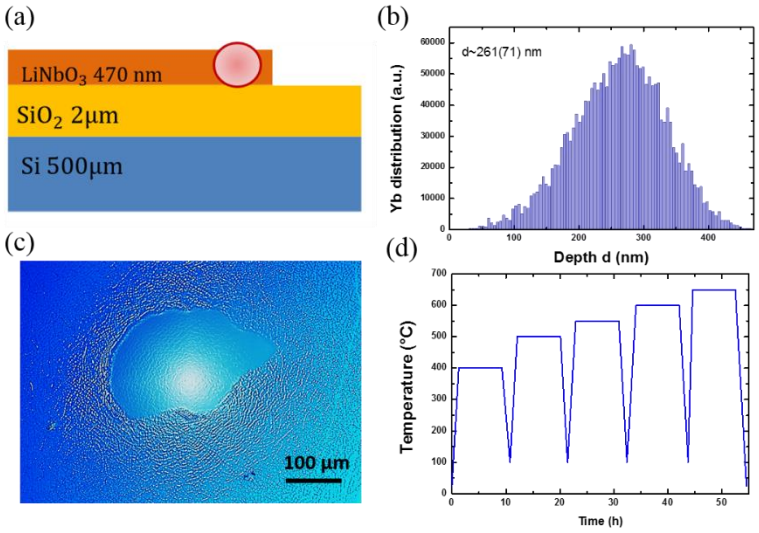

Fig. S4. *Yb3+ ion implantation. (a) Cross-section of the LN thin film. The implanted Yb is mainly located at the center of the LN layer. (b) The SRIM simulation with 1.5 MeV implantation energy. (c) Optical image of the cracked LN thin film after annealing at 750 degrees. (d) The annealing protocol in this experiment.*

3. Sample fabrication for long waveguide and microdisk cavities

A 3-inch diameter NANO LN z-cut wafer was cut in smaller chips of some millimeters. Chips were cleaned in a Piranha solution(sulfuric acid, H_2 SO_4, and hydrogen peroxide, H_2 O_2, in ratio 3:1) for a few minutes and then washed in H_2O and rinsed in isopropanol solvent. A 30 nm layer of titanium(Ti) was evaporated using e-gun technique. In order to fabricate structures on the top of the film a double layer of polymethyl methacrylate (PMMA) were spin-coated. The bottom layer had a molecular weight of 200 K while the top had 950 K. Since the two layers needed different exposure energies, they resulted in different gaps (as shown in Fig S5 (b).) preventing eventual bridges between the top and bottom layer in the subsequent evaporation. The e-beam lithography was changed according to which structures were necessary to be realized. For the long waveguide (see Fig. S7), since they were supposed to be mm-size long and stitches needed to be avoided, Fix Beam Moving Stage (FBMS) technique was involved. A dose of 220 $\mu C/cm^2$ was chosen for all the waveguides. For the microdisk cavities, instead, the common technique (Fixed

stage, moving gun) was used and sweep of dose from 180 $\mu C/cm^2$ to 220 $\mu C/cm^2$ with a step of 10 $\mu C/cm^2$ while sweeping the gap between the waveguide and the microdisk was selected.

After the development in methyl isobutyl ketone (MIBK) and isopropanol (1:3), a layer of 120 nm of nickel-chromium(NiCr) was e-gun evaporated and the lift off was executed in n-ethylpyrrolidone (NEP) at 90 °C for several minutes.

The NiCr mask was then transferred into the sample by dry etching in a Plasma Oxford Instruments machine. The etching was divided into two main parts. The first part consisted of a mix of SF_6 and Ar-milling. Starting with SF_6-gas with RF and ICP for two minutes, the sample was then smoothed with Ar-milling for 1 minute without the use of ICP. Afterwards, the sample was cleaned from the residual hard mask in a solution of Nitric acid and Chromium etcher and eventually again in Piranha to remove Ti layer. The last part of the etching consisted of two steps of Ar-milling for 2 minutes each.

At the end of the process, sample was further cleaned in Piranha solution.

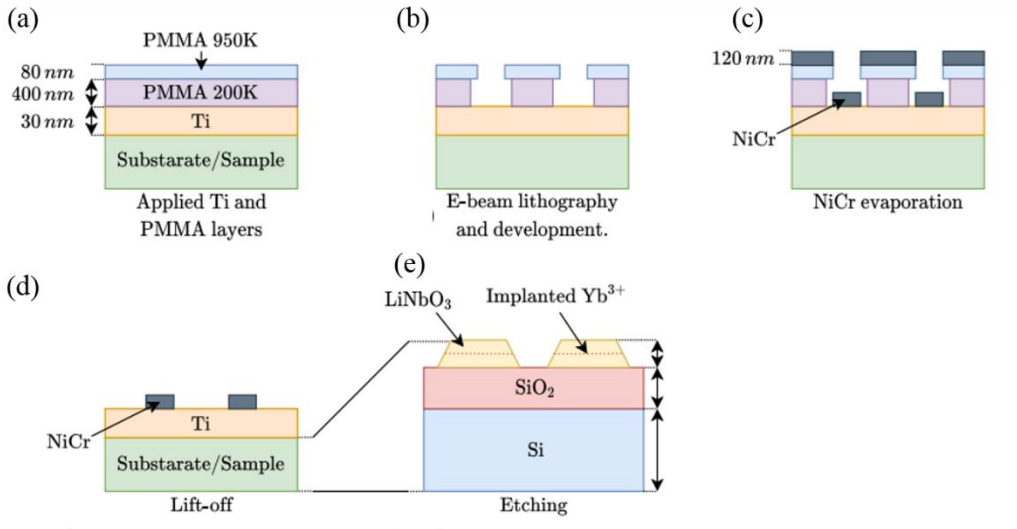

Fig. S5.
Fabrication protocol of Yb:LN microstructures. (a) Sample after applying the Ti and PMMA layers. (b) Sample after E-beam lithography and development. (c) Sample after NiCr evaporation. (d) Sample after PMMA lift-off. (e) Sample after chemical and mechanical etching.

The microdisk cavities required further steps for depositing the electrodes. After the creation of photonic devices in the LN film, they were encapsulated in SU8. The SU8 is spin coated with a thickness of 1 µm. The ends of the waveguides were opened to couple the light in and out from the waveguides(Fig S4.).

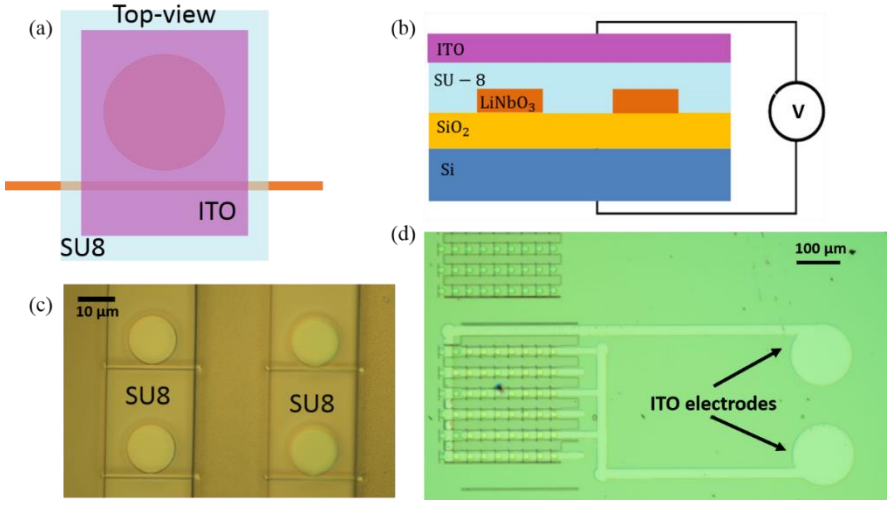

Fig. S6.
Fabricated structure with electrodes. (a) Top view image of the schematic diagram. (b) Cross-section of the schematic diagram. (c) Microscopic image of the fabricated structure (top view). (d) Overview image of the fabricated structures (top-view).

The last step consisted of another photolithography in which ITO electrodes were deposited The design and microscope images of the fabricated waveguide-resonator structure is shown in Fig S6 and it was eventually mounted on a cold finger of the cryostat.

To increase the collection efficiency of the microscopy, we undercut the ends of the waveguides (both short and long ones) at 45 ° as shown in Fig. S7. According to COMSOL simulation, the maximum collection efficiency was calculated to be 60%. In the experiment, we achieve 30% collection efficiency.

The Q-factor of the microdisk is: $\frac{1}{Q} = \frac{1}{Q_{mat}} + \frac{1}{Q_{rad}} + \frac{1}{Q_{Scat}}$, where Q_{mat} is determined by intrinsic absorption and scattering of the resonator material ($>10^7$ in LN) Q_{rad} is the radiative quality factor, and Q_{scat} is the surface absorption and scattering of the cavities. Q_{rad} = RE k/ 2Im k. According to the simulation, as shown in Fig. S7 (e), the Q_{rad} in the experimental geometry is more than 10^9. Hence, the Q-factor of the microdisks in the experiment is mainly limited by the scattering loss of the cavities. It can be improved by further optimizing the fabrication protocol.

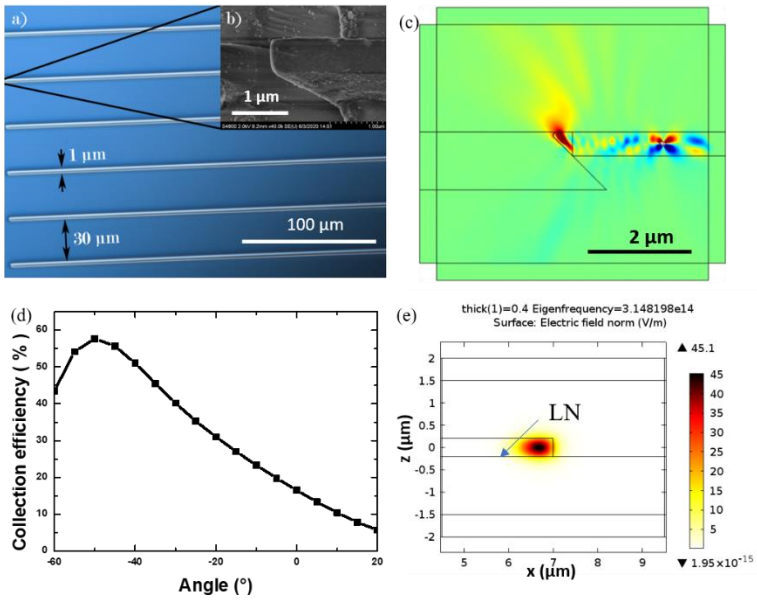

Fig. S7.
(a) Microscopic image of the fabricated long waveguide. (b) SEM image of the 45 degrees undercut end of the waveguide. (c) COMSOL simulation of the 45 degrees undercut. (d) The collection efficiency corresponds to the angle of the undercut. (e)COMSOL simulation of the microdisk with the experimental geometry.

4. Spectroscopic study of Yb^{3+} in LN

(1) Emission spectra of implanted and native Yb^{3+} in LN

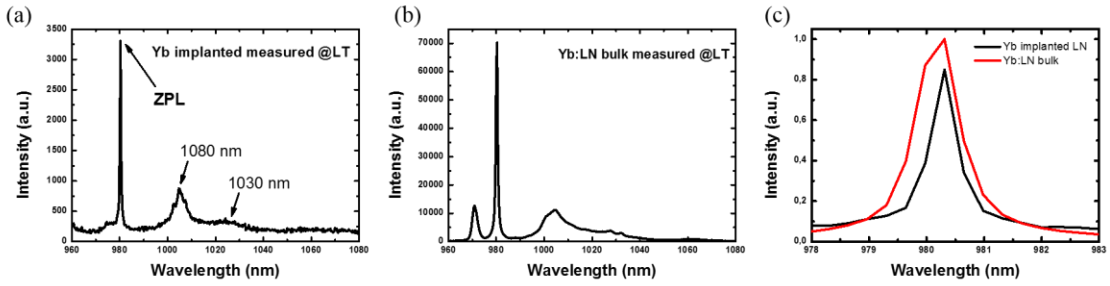

Fig. S8. *(a) The emission spectrum of the implanted Yb:LN long waveguide measured at 3.5 K. (b) Emission spectrum of the bulk Yb:LN measured at 3.5 K. (c) Zoom in image of both samples at ZPL positions.*

After the annealing of implanted Yb:LN, we measured the emission spectra (obtained by Ocean Optics, QE PRO) of both implanted Yb:LN long waveguide (see Fig. S7) and Yb:LN bulk crystal(congruent LN, Czochralski growth, Mg 6% , Yb 0.01% concentration) at cryogenic temperature. It is shown in Fig. S8 that both samples exhibit a sharp ZPL at 980 nm in the spectra.

The ZPLs of the two spectra overlap well. It indicates that the implanted Yb^{3+} in LN presents similar emission spectrum in comparison with Yb^{3+}:LN bulk crystal.

(2) Hole burning spectroscopy of Yb^{3+}:LN

The spectral hole burning was first performed in Yb:LN bulk crystal. The measurement was taken at cryogenic temperature (~3.5 K) and zero magnetic field. The result is plotted in Fig. S9 (a). It shows two overlapping holes. The measurement data is best fitted with a double Gaussian, where the FWHM of the 1st Gaussian is 58 MHz and 6MHz of the 2nd Gaussian. The double hole appearance could have several reasons. One explanation could be given by the fact that the isotopes ^{171}Yb and ^{173}Yb possess nuclear spins. Those different isotopes could interact differently with the environment and therefore lead to a narrower homogeneous broadening, which would be observed in the hole burning measurement as the 2nd hole [24]. Another explanation would be the different positioning of the Yb^{3+} ions inside the lattice. Therefore the Yb^{3+} ions experience a different intensity of the fluctuating magnetic field produced by the LN crystal atoms. This could lead to a narrower homogeneous linewidth.

The measured hole burning spectrum of implanted Yb:LN long waveguide is shown in Fig. S9 (b). The spectrum is similar to the Yb:LN-bulk measurement, where two overlapping holes have been observed. The spectral hole width of the 1st Gaussian is 82 ± 1MHz the 2nd Gaussian has a width of 8 ± 1MHz. The corresponding contrasts are h1 ≈ 21 % and h2 ≈ 6%. According to the spectral hole width, the optical properties of Yb implanted:LN is similar to the native Yb doped LN bulk crystal. We can deduce that 650 degrees post-annealing is sufficient to stabilize implanted Yb ions and recover the damage of the thin film.

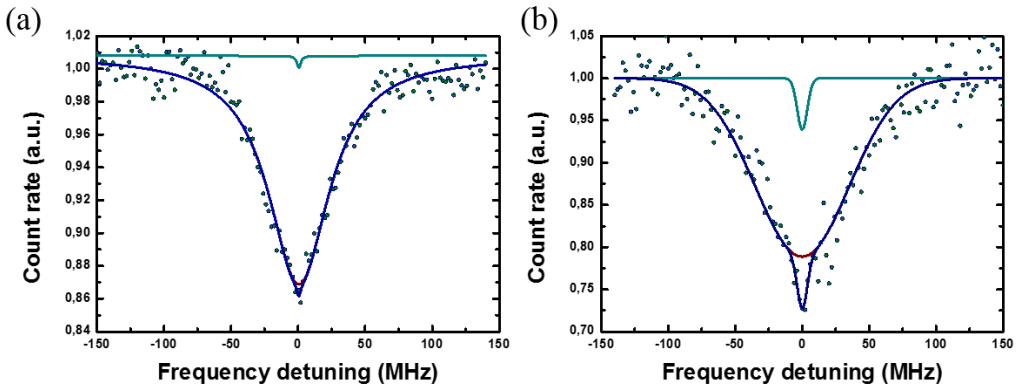

Fig. S9.
(a) Spectral hole burning of the bulk Yb:LN at 3.5 K and zero magnetic field. (b) Spectral hole burning of the implanted Yb in LN long waveguide at 3.5 K and zero magnetic field.

(3) Temperature dependence of the spectral hole width

The contrast and the FWHM of the spectral holes strongly depend on environmental influences. Changing the temperature of the sample results in the change of the spectral hole shape, due to the changing of spin-lattice relaxation. There are multiple mechanisms causing spin-lattice relaxation, including direct relaxation, Raman relaxation, fast Orbach relaxation or a combination of them. They can be described by

$$F\{\omega_n(T\} = a_0 \cdot T \quad \text{(direct relaxation)}$$

$$F\{\omega_n(T\} = a_1 \cdot e^{-\frac{\Delta E}{k_b T}} + c_1 \quad \text{(Raman relaxation)}$$

$$F\{\omega_n(T\} = a_2 \cdot T^n + c_2 \quad \text{(Orbach relaxation)}$$

and can be combined to:

$$\frac{1}{T_1} = \omega_n = a_0 \cdot T + a_1 \cdot e^{-\frac{\Delta E}{k_b T}} + a_2 \cdot T^n + c.$$

where k_b is the Boltzmann constant, and ΔE is the energy difference between the two lowest energy states in the system. Nevertheless, the fact that these effects are occurring in a combined fashion, single ones can dominate the result. Figure S10 shows the measured temperature dependence of the linewidth ω_1 fitted with the functions of Raman relaxation and Orbach relaxation. Both curves fit the data reasonably well. According to the fitted data, we deduced the $\Delta E = 34 \pm 5\ \mathrm{cm}^{-1}$ in the Orbach relaxation. However, the literature value for Yb:LN is $\Delta E_{literature} = 264\ \mathrm{cm}^{-1}$ [36]. Therefore, Orbach relaxation is unlikely to be the dominant factor in

broadening the spectral hole width ω_1. That also suggests that Raman relaxation, with an exponent of $n = 3.5 \pm 0.5$, plays a dominating role in this process at 3 K- 20 K temperature range.

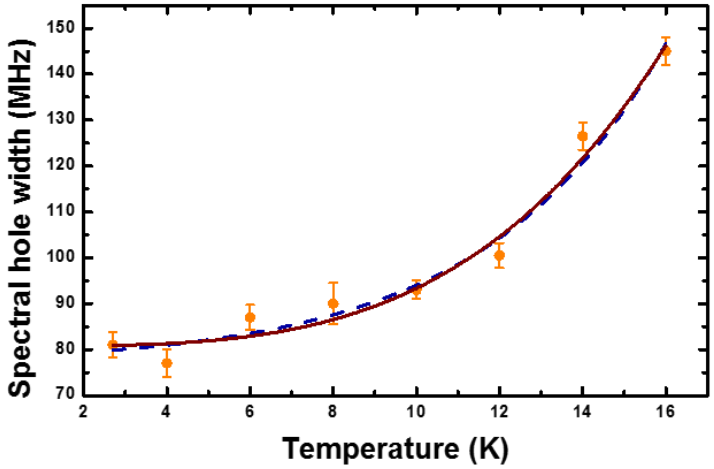

Fig. S10.
Temperature dependence of the linewidth $\boldsymbol{\omega_1}$ *measured from spectral hole burning of Yb:LN-waveguide, with the fitted temperature dependence of Raman and Orbach relaxation.*

5. Purcell enhancement model and cQED parameters estimation

The fluorescence decay curve was modeled using the following model. While decaying, an ion at the location (r,z) within the cavity mode will emit into the cavity mode with the probability $\gamma(r,z)/(\gamma(r,z)+\Gamma_0)$. Here, r and z are the radial and the axial coordinates of the ion within the cavity mode, $\gamma(r,z)$ is the local decay rate due to Purcell effect, and Γ_0 is the intrinsic decay rate corresponding to the waveguide lifetime of 430µs. At the same time, the probability to excite the ion is proportional to the same ratio. Finally, the chances of finding an ion at the location (r,z) are proportional to the density distribution of the implanted ions $n(z)$. The latter is obviously independent of the radial coordinate. The radius of the cavity (7µm) is much greater than the radial size of the mode (≈0.5µm), therefore, integrating the

contributions of the ions from the whole 3D mode volume is equivalent to integrating over 2D radial cross-section.

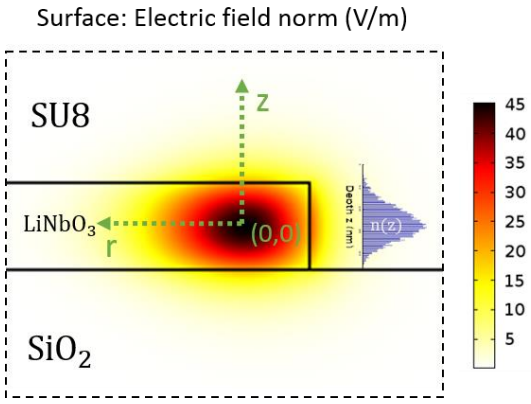

Figure S11.
Slice along z direction and zoom of the cavity mode to represent how the mode and the distribution of ions given by implantation are modeled to achieve a better estimation of the Purcell enhancement.

Combining all three ingredients, we obtain the following shape of the decay curve:

$$I(t) = B + A \oint \left(\frac{\gamma(r,z)}{\gamma(r,z) + \Gamma_0} \right)^2 n(z) \exp(-(\gamma(r,z) + \Gamma_0)t)\, drdz$$

where integration is done within the cross-section of the mode. Here A is the normalization coefficient and B is the background noise. In turn, $\gamma(r,z)$ can be modeled as follows:

$$\gamma(r,z) = \gamma_0 exp\left(-\left(\frac{z - z_C}{w_z} \right)^2 - \left(\frac{r - r_C}{w_r} \right)^2 \right)$$

where γ_0 is the Purcell decay rate at the very center of the mode, $w_{z,r}$ are the Gaussian half-widths of the mode in axial and radial directions respectively, and z_C and r_C are the coordinates of the mode center. The model widths can be obtained from the finite element simulation and appear to be $0.18\ \mu m$ and $0.24 \mu\ m$ respectively. The distribution of implanted ions is simulated using SRIM (Stopping Range of Ions in Matter) software. In the end, the model uses only 3 free parameters: the overall scaling A, the overall background B,

and the maximum Purcell decay rate γ_0. Fitting the decay data with this model resulted in γ_0=10.24

In order to estimate the QED parameters the follow theory has been followed:

The Purcell enhancement is described as

$$P = \frac{4g^2}{(\kappa\Gamma_0)}$$

Where g is the Rabi frequency, κ is decay rate of the cavity and Γ_0 is the spontaneous emission. Taking in account a cavity with a Q-factor of ~79833, the decay rate κ = 3.83 GHz, resulting in a g = 2π×1.9 MHz. The QED cavity actively affects the Yb:LNOI fluorescence, leading the emission of photons of Yb into the cavity mode with a probability:

$$\beta = \frac{P}{P+1}$$

The measured probability corresponds to 91,1%.

Moreover the initial branching ratio for the ground state of Ytterbium is ζ=0.25, given by a crystal field splitting of the ground state ${}^2F_{\frac{7}{2}}$ into 4 kramers levels, and this is improved to 93.3%, calculated by

$$\zeta_c = \zeta \frac{P_0 + 1}{\zeta P_0 + 1}$$

Where $P_0 = P/\zeta$ and P is the effective Purcell coefficient, $P = P_0\zeta = \frac{\tau}{\tau_0} - 1$.

6. Cavity performance

Cavities were pre-characterized in the frequency domain at room temperature, offering a wide spectrum of choices for the most adequate wavelength. The natural wavelength of cavities was always around 980 nm, starting from 970 nm up to 986 nm. Given our electro-optic tuning of 0.5 nm in total (160 GHz), two cavities were selected for the subsequent experiments of Yb^{3+} ions

inside the cavities. The cavity in FigS11(a) was characterized in the set-up described in Note 1. Two convoluted Lorentzian peaks well fitted the Fluorescence intensity spectrum, which resulted in a Q-factor of 79,833. The second cavity was, instead, characterized by sweeping the frequency of 980 nm tunable diode in the range of 60 GHz in the set-up described by S1. Repeating the same Lorentzian fit, two convoluted peaks were fitted, giving a Q-factor of 64,065.

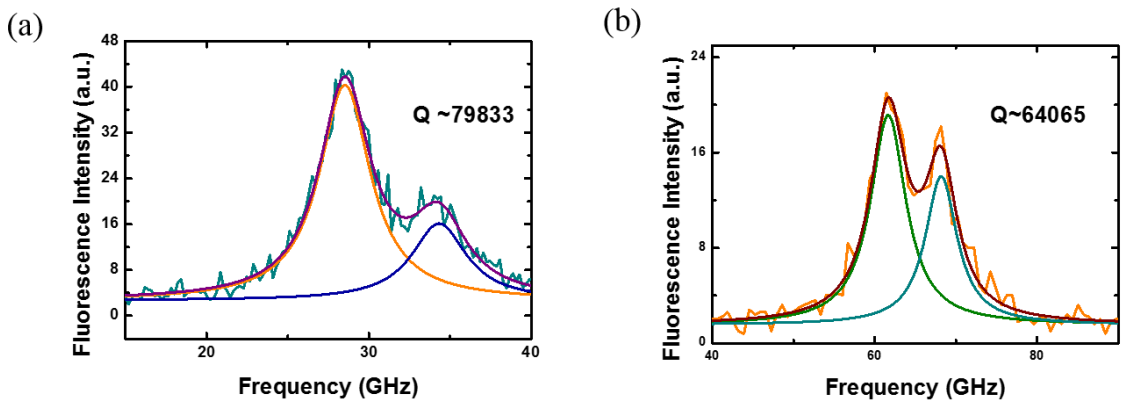

Fig. S12.
Q factor measurements (a) The cavity studied in Fig. 2 in the main text. (b) The cavity studied in Fig. 3 in the main text.

After calculation of the Q-factor, we needed to estimate how the cavity was effectively shortening the lifetime of the implanted ions.

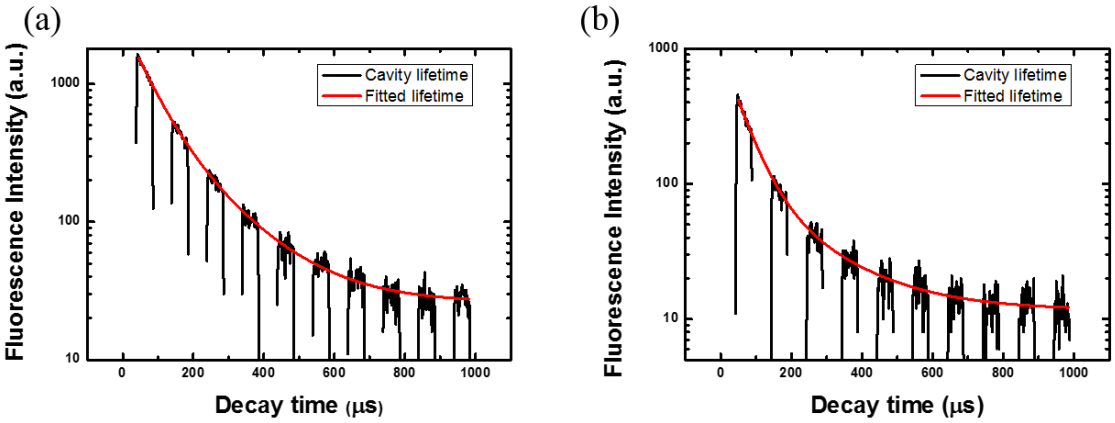

Fig. S13.
Purcell enhancement and lifetime measurement. (a) Lifetime measurement of cavity Fig. S11 (a). (b) Lifetime measurement of cavity Fig. S11 (b).

The last step of the experiment was to investigate the PLE spectra of different cavities at different temperatures.

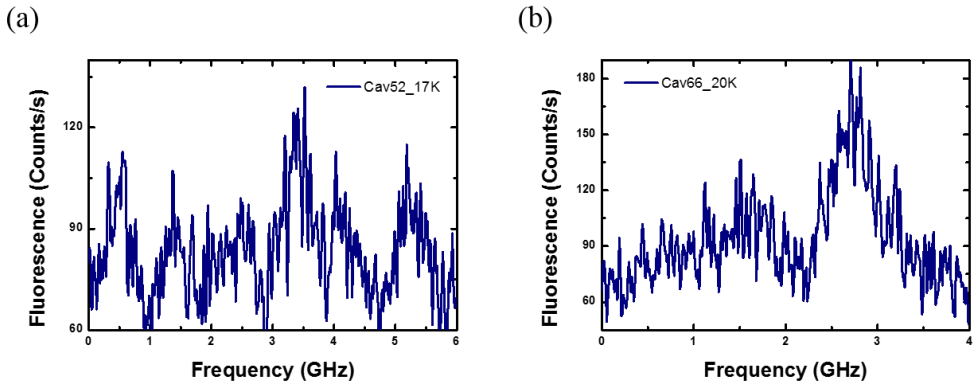

Fig. S14.
Evidence of single $\mathbf{Yb^{3+}}$ *ions in different cavities at two different temperatures(17 K and 20 K).*

In Figure S14, two PLE spectra at 17 K and 20 K of different cavities are shown. In both cases, it is possible to distinguish discrete peaks from the spectral background, confirming that peaks are not artefacts from the measurements devices but Yb^{3+} ions signals.

We further show the linewidth statistic of the discrete lines plotted in Fig. 3 (b). The average linewidth is $2\pi\times247\pm9$ MHz.

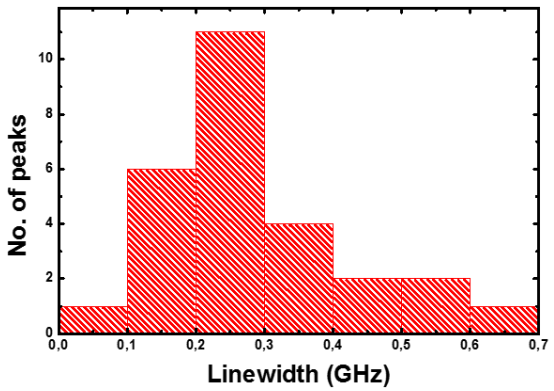

Fig. S15. *Linewidth statistics of the discrete peaks in Fig. 3b.*

References

1. Homogeneous linewidth measurements of Yb3+ ions in congruent and stoichiometric lithium niobate crystals. Z. Kis, G. Mandula, K. Lengyel, I. Hajdara, L. Kovacs, M. Imlau,. s.l. : Opt. Mater, 2014, Vols. 845,
2. New low symmetry centres of Yb3+ impurities in lithium niobate single crystal. T. Bodziony, Opt Mater, 2007.